Extended states of nonlinear traveling-wave convection. II. Fronts and spatiotemporal defects

Paul Kolodner
A T & T Bell Laboratories, Murray Hill, New Jersey 07974-0636
(Received 1 June 1992)

This paper continues a description of experiments on one-dimensional, nonlinear, traveling-wave convection in a binary fluid with separation ratio $\psi = -0.127$ in a narrow annular cell. It is possible to create and manipulate steady-state sources and sinks of traveling waves in this system, as well as to produce stable fronts that separate convecting and quiescent regions. Source defects tend to drift at constant velocity, emitting Doppler-shifted traveling waves whose wave number lies outside the Eckhaus boundary measured for spatially uniform traveling-wave states. I present both qualitative descriptions of such phenomena and quantitative measurements of the amplitude and wave-number profiles of sources, sinks, and fronts.

PACS number(s): 47.25.Qv, 47.20.Ky

I. INTRODUCTION

The past 15 years have seen much progress in the understanding of the physics of pattern formation. Much of this advancement has been the result of careful study of model systems—both experimental and theoretical—which exhibit bifurcations to periodic patterns of high symmetry in one or two dimensions. A classical example is Taylor-Couette flow, in which toroidal vortices are formed in the fluid which fills the gap between counterrotating cylinders. In a Taylor-Couette apparatus with a ramped gap, the axial wave number of the vortex pattern is selected exactly, in a way which has been explained by theory in quantitative detail [1,2]. In the previous paper of this pair [3] (referred to as I in the following), I described another example of the reduction of pattern-formation physics to a system exhibiting a highly symmetric state: measurements of the dispersive and stability properties of spatially uniform traveling waves (TW) of convection in a binary fluid in a periodic, one-dimensional system.

Despite the utility of studying highly symmetric patterns of reduced dimensionality, most patterns in nature are not so regular. In typical systems which exhibit a transition to a periodic pattern, states of high symmetry are usually disrupted by real-space defects. In convection in thin layers of pure fluids, for example, patterns exhibit a narrow band of wave numbers, but boundary effects cause these patterns to exhibit a high density of defects, even at onset [4]. Electrohydrodynamic convection in thin layers of liquid crystals presents another example. Because of the anisotropy of the fluid, and because a huge lateral aspect ratio can be obtained, this system can be used to create large patterns of one-dimensional stripes [5]. However, such experiments quite typically also produce erratic, high-defect-density states [6], and a statistical description of the defect evolution has superceded theories of the stability of symmetric patterns as the appropriate description of such states [7,8].

In a single spatial dimension, defect behavior can be much less complicated. In a one-dimensional system which exhibits a bifurcation to a steady, periodic pattern, there are essentially only two defects possible: spatial variations of the amplitude—such as fronts—and of the wave number. The latter type of defect has been observed in experiments on long chains of rolls in slot convection [9] and has been discussed theoretically using the concepts of phase dynamics [10]. In one-dimensional systems which exhibit a bifurcation to an oscillatory state, defect behavior can regain some of the complexity seen in two-dimensional patterns, since defects can now be formed in two-dimensional space-time. The spatiotemporal analogs of dislocations, grain boundaries, and other real-space defects have been observed in experiments on one-dimensional TW convection in binary fluid mixtures [11] and in liquid crystals [12], as well as in the "printer's instability"—the flow in the opening gap between two counterrotating, nonconcentric cylinders [13]. In recent experiments on forced convection in pure fluids, the cross-roll instability [14] was exploited to create TW states that exhibited source defects [15].

Despite the ubiquity and importance of real-space defects in two-dimensional patterns and of spatiotemporal defects in one-dimensional TW systems, the behavior of isolated defects has received very little experimental attention. Pocheau and Croquette studied the climb of real-space dislocations in an otherwise one-dimensional pattern of steady convective rolls in a pure fluid [16], and Yang, Joets, and Ribotta documented the formation of isolated dislocations in convection in liquid crystals [17]. Goren *et al.* [8] and Rasenat, Steinberg, and Rehberg [18] also studied dislocations in convection in liquid crystals, this time focusing on the attraction of nearby defects. While the amplitude structure of real-space dislocations was measured by the authors of Ref. [18], the structure of spatiotemporal defects of TW seems never to have been the subject of careful experimental study.

Quantitative characterization of the structure of steady-state spatiotemporal defects in a one-dimensional TW system is the subject of the present paper. The experimental system is TW convection in an ethanol/water mixture in a narrow, annular container. As described in

I, this system exhibits slow, nonlinear TW which propagate azimuthally around the annulus. In I, I described the dispersive and stability properties of these TW in some detail. In the present paper, using the same fluid and apparatus, I demonstrate experimental techniques with which these TW can be made to exhibit steady spatiotemporal defects—sources, sinks, and fronts—and with which these defects can be manipulated—i.e., moved, annihilated, or transformed. I also present quantitative measurements of the amplitude and wave-number profiles of these defects. These experiments have been performed in an extremely stable and uniform convection cell, and the diagnostics used to analyze the flow structure are extremely precise.

This paper is organized in the following manner. Section II is a brief review of the apparatus and procedures used in the experiments. Sections III and IV then describe techniques used to produce and manipulate TW fronts and source and sink states, respectively. In Sec. V, I present quantitative measurements of defect structure. Section VI describes further qualitative observations of defect behavior, and Sec. VII is a discussion

II. REVIEW OF APPARATUS AND PROCEDURES

The apparatus used in these experiments is identical to that used in I, and the experiments described in these two papers were performed during the same six-month time period. The cell is an annulus of height $d=0.2737$ cm with dimensionless radial width and mean circumference 1.677 and 82.47, respectively. The cell is heated from below and cooled and visualized from above. The fluid is the same ethanol and water mixture used in I, with separation ratio $\psi=-0.127$, Prandtl number 6.86, and Lewis number 0.0083. The spatial uniformity and temporal stability of the Rayleigh number in this apparatus were 3×10^{-4} and 3×10^{-5}, respectively. The Rayleigh number has been calibrated with an absolute uncertainty of about $\pm2\%$; scatter and drifts in the Rayleigh-number measurements were corrected to a level of $\lesssim2\times10^{-4}$. As in I, Rayleigh numbers have been normalized by the critical Rayleigh number for the onset of steady convection in a pure fluid in a laterally infinite layer. Rayleigh numbers are quoted to five digits, and the error reported in parentheses represents the random component of the uncertainty.

Particular care was taken in this series of experiments to ensure that the shadowgraphic flow-visualization system operated in the linear regime, so that quantitative measurements of the structure of TW states could be made. Full complex demodulation of the shadowgraph data was used to compute maps of the amplitude and wave-number profiles of the two azimuthally propagating TW components [19]. The distortion-correction procedures described in I and in Ref. [19] were used, so that the computed amplitude (wave number) profiles were accurate to within about $\pm5\%$ ($\pm1\%$). Since the optical distortions which impose these limits tend to appear at random, slowly drifting locations in the shadowgraph image, and since the defects under study often appeared at different locations, it has been possible in many cases to reduce these numbers substantially by averaging.

When quantitative flow visualization is under discussion, the question of spatial resolution must be addressed. In the present case, the resolution can be limited by three effects: blur in the optical system, finite spatial density of pixels in the imaging camera, and lowpass filtering in the data processing. The blur is quite difficult to assess quantitatively. However, on increasing the focalization distance of the optical system into the nonlinear regime, second, third, and higher harmonics are observed to appear in the spatial spectrum of a pattern of spatially uniform TW. In the actual images, the roll boundaries develop the caustic profiles characteristic of nonlinear shadowgraph images [20]. These observations suggest that the blur affects only length scales smaller than one wavelength of the pattern. Likewise, the pixel spacing is quite small: The images were recorded on a mesh of 1 pixel per degree of angle, or approximately 9 pixels per TW wavelength. Finally, a too-narrow demodulator bandwidth can obviously smooth out a spatially varying amplitude or wave-number profile. This effect was assessed by performing the demodulation on selected data files using several different bandwidths. As expected, decreasing the bandwidth below some threshold causes the profiles to be increasingly smooth, while increasing the bandwidth beyond the threshold merely adds noise without sharpening up the profile. I typically used bandwidths which were somewhat wider than the threshold observed for the sharpest profiles measured for a given type of defect. Interestingly, wave-number profiles can be computed without distortion using narrower demodulator bandwidth than can amplitude profiles. The wave-number and amplitude profiles discussed in this paper were computed separately to take advantage of this. The sharpest amplitude feature observed in these experiments exhibited a (10–90)% width of approximately 3 times the cell height, and this appears to be the true shape of the convective profile, unaffected by the resolution of the optics and signal processing.

III. PRODUCTION AND CHARACTERIZATION OF FRONTS OF TRAVELING WAVES

Stable defects do not happen by accident. In experiments at $\psi=-0.25$ in a large annulus, we found that simply turning the Rayleigh number above onset triggers a complicated transient which leads to a state of slow TW which fill the cell [11]. For the fluid used in the present experiments, a similar transient is seen, but the final state usually consists of one or a few TW pulses, since pulses are stable just above onset at this value of ψ [21,22]. As demonstrated in I, pulse formation can be prevented if the system is first prepared in a spatially uniform state of unidirectional linear TW. In that case, if the cell is sufficiently uniform, then the first state to evolve upon raising the system above onset is again a spatially uniform state of slow, nonlinear TW.

Producing stable spatiotemporal defects has required further development of the pulse-launching and local-heating techniques that were introduced in Ref. [23] and refined in Ref. [22]. Figure 1 illustrates how these tech-

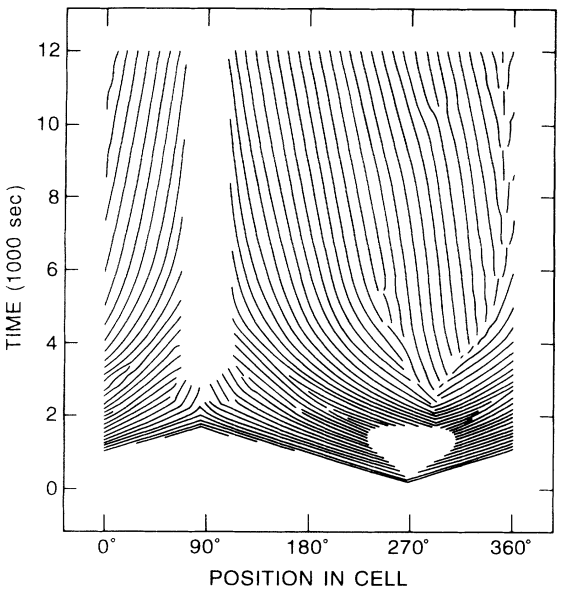

FIG 1. The formation of a source-front state is illustrated by a graph of the spacetime trajectories of roll boundaries. Initially, a disturbance was created at location 270°, triggering fast, outwardly propagating, linear TW which form the seed of a source defect. After these wave packets had propagated about 90°, the Rayleigh number was increased, and extra heat was applied on the right side of the system, in the region centered at location 270°. The general increase of the Rayleigh number caused the linear TW to slow down, and the extra local heating near 270° caused the blank region there to fill up with TW, forming a source defect. The final state of the system consists of time-dependent spatiotemporal defects, at Rayleigh number $r=1.261\,45$.

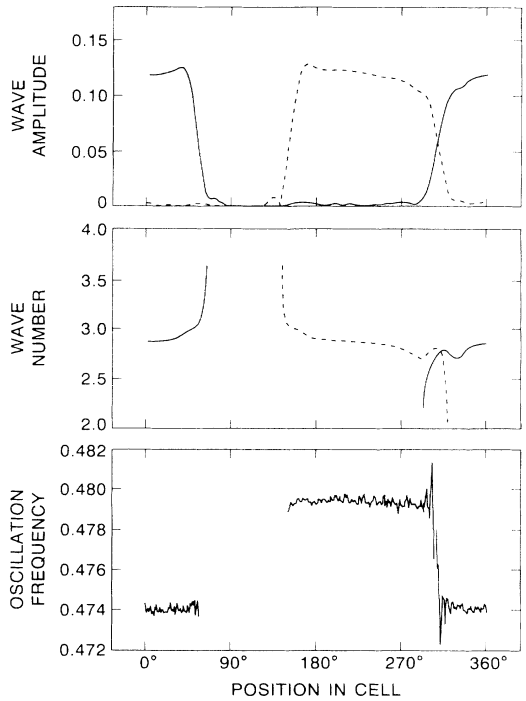

FIG. 2. Top and middle frames: The spatial profiles of the TW amplitude and wave number, as computed using complex demodulation, are shown for the source-front state produced in Fig. 1. Solid (dashed) curves correspond to the right (left) propagation direction. Bottom frame: spatial dependence of the temporal oscillation frequency. Because the source drifts slowly to the left (dimensionless source velocity $v_s=-0.001\,04$), the frequencies of left- and right-going TW are Doppler shifted. Reduced Rayleigh number: $r=1.258\,92$.

niques can be used to create a defect state. At the beginning of this run, the Rayleigh number was raised just above onset ($r_{co}=1.291\,33$), and a small distance was created at location 270°, as in Ref. [23]. This disturbance decomposed into a pair of growing, outwardly propagating linear wave packets. When these had propagated about $\frac{1}{4}$ of the circumference of the cell (this took about 30 min), the Rayleigh number was abruptly increased, causing the system to evolve into a nonlinear state. Under normal circumstances, this would have resulted in the formation of two oppositely propagating pulses near locations 180° and 360°. To prevent this, I applied a strong Rayleigh-number gradient by turning on point heat sources on the underside of the cell, in a 75°-wide region centered at location 270°. As shown by the heart-shaped blank spot in Fig. 1, this caused that region to fill with oppositely propagating TW, forming a source defect. From its initial position at location 290°, the source drifted to the right and then came to rest at location 350°. At the opposite side of the cell, because no local heating was applied, the tendency of the TW in this system to form confined states caused a quiescent region to open up. This blank spot rapidly stabilized. The final steady state consists of a motionless source and a pair of leading-edge fronts (i.e, fronts *into which* TW propagate). I refer to this as a source-front state.

The top two frames of Fig. 2 show the amplitude and wave-number profiles of the two TW components in this state, computed using complex demodulation. The source consists of a region in which left and right TW have comparable amplitudes, growing rather rapidly from zero amplitude. Outside the core of the defect, the TW amplitudes saturate but continue to grow slightly as a function of distance from the source. At the fronts, both wave amplitudes drop abruptly to zero. In regions where the TW amplitudes are not rapidly varying in space, the wave-number profiles are almost flat. In Sec. V below, these amplitude and wave-number profiles are analyzed in detail. As seen in the bottom frame of Fig. 2, the temporal oscillation frequency is not the same everywhere in the system: Left-going TW travel faster than right-going TW. As shown in Sec. IV below, this is a Doppler shift caused by slow source motion.

The source-front states in Figs. 1 and 2 appear to be identical to the "neutrally stable fronts" observed previously in experiments at two different separation ratios in rectangular cells [24]. As in that work, the fronts are observed to move with a velocity v_{fr} that depends on Rayleigh number, as illustrated in Fig. 3. Note that the source appears to be unaffected by the small changes in r

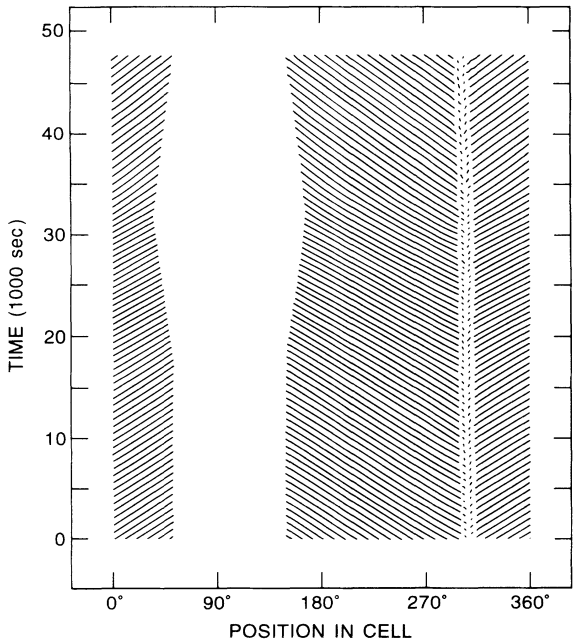

FIG. 3 Space-time trajectories of the roll boundaries are shown for the source-front state of Figs. 1 and 2 during a run in which the Rayleigh number was changed. Initially, $r = 1.258\,92$, close to the neutral-stability point $r_v = 1.258\,85$. At time $t = 16\,560$ sec, r was reduced to $r = 1.255\,98$, and the fronts receded with constant velocity. Then, at $t = 31\,040$ sec, r was increased to $r = 1.261\,80$, causing the fronts to advance into the quiescent region. These small changes in Rayleigh number had little effect on the source defect.

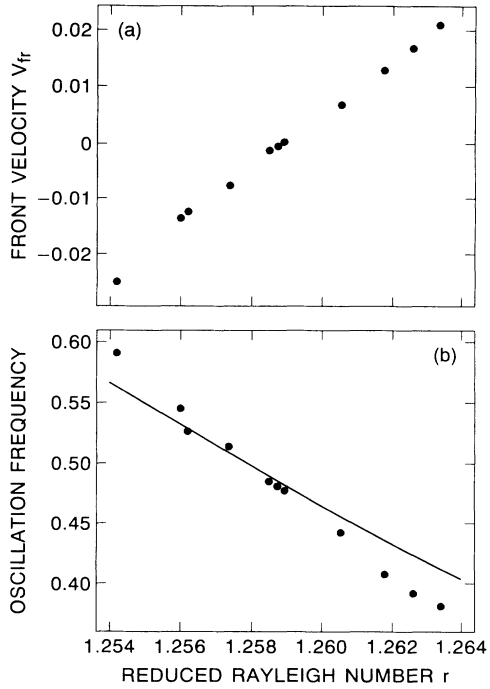

FIG 4. (a) The front velocity v_{fr} is plotted as a function of Rayleigh number, as determined by measurements like that in Fig. 3. In the center of the graph, $v_{fr}(r)$ passes linearly through zero at $r_v = 1.258\,85(3)$, with slope $dv_{fr}/dr = 4.127(33)$. (b) The solid symbols represent measurements of the spatially averaged oscillation frequency of source-front states as a function of Rayleigh number. The solid curve shows the frequency of the $n = 40$ spatially uniform TW state reported in I.

in this run (but compare Fig. 23 below). Figure 4 shows the Rayleigh-number dependences of the front velocity and the spatially averaged oscillation frequency. The latter decreases with r, exhibiting a slightly different dependence on r than the spatially uniform TW studied in I [solid curve in Fig. 4(b)]. The front velocity decreases linearly with r, passing through zero at $r_v = 1.258\,85(3)$ with slope $dv_{fr}/dr = 4.13(3)$. r_v lies just above the saddle-node Rayleigh number $r_s = 1.226\,43(10)$ measured in I.

Measurements of the properties of neutrally stable fronts in both geometries are gathered in Table I. Comparing these results is somewhat difficult, not because of the difference in geometry but because of the difference in cell width Γ_y, which has a poorly understood effect on most of the measurements. (By contrast, the finite *length* of the rectangular cells affects only the onset Rayleigh number r_{co}, and this effect is understood quantitatively

TABLE I. Neutrally stable fronts.

ψ	width[a]	r_{co}[b]	r_v[c]	r_s[d]	r_{co}^{∞}[e]	r_v^{∞}	r_s^{∞}	$\frac{dv_{fr}}{dr}^{\infty}$	k[f]	$v_{ph}(r_v)$[g]
−0.408	3.00	1.6976(1)	1.4049(1)	1.339(8)	1.6601	1.3739	1.309	1.022(20)	2.70–2.80	0.553(10)
−0.240	3.00	1.3555(2)	1.2630(2)	1.254(4)	1.3256	1.2351	1.226	1.94(20)	2.65–2.75	0.555(10)
−0.127	1.677	1.2913(3)	1.258 85(3)	1.2259(1)	1.1354	1.106 95	1.0780	4.69(4)	2.80–2.90	0.163(3)

[a]The cell width Γ_y is measured in units of the cell height. The $\Gamma_y = 3.00$ results were measured in a rectangle cell and are taken from Ref. [24]. The $\Gamma_y = 1.677$ results were measured in the present experiments.

[b]For the rectangular-cell measurements, the onset Rayleigh number r_{co} has been extrapolated to infinite cell length using the measurements of Ref. [25].

[c] r_v is the measured value of the reduced Rayleigh number at which the front velocity is zero.

[d]For the present experiments, r_s is the saddle-node Rayleigh number measured in I. For the rectangular-cell measurements, r_s is the measured Rayleigh number below which nonlinear TW are not stable. This probably does not correspond to the true saddle node.

[e]The superscript ∞ represents measurements in which the Rayleigh number has been corrected for the effect of finite cell width using the linear-state measurements in Ref. [26], as described in the text.

[f] k represents the range of wave numbers measured at various spatial positions.

[g] $v_{ph}(r_v)$ is the TW phase velocity measured at Rayleigh number r_v.

[25]. The rectangular-cell onset measurements in the third column in Table I have been extrapolated to infinite cell length for comparison with the new annulus results.) To make a rough correction for cell width, the Rayleigh-number measurements presented in columns 3–5 of Table I can be divided by $\alpha(\Gamma_y)=1.1373$ (1.0226) for $\Gamma_y=1.677$ (3.00), which is the measured factor by which the finite cell width suppresses the onset Rayleigh number [26]. These results, distinguished with a superscript ∞, are presented in columns 6–8 of Table I. The velocity derivative $dv_{\rm fr}/dr^{\infty}$ in column 9 of the table has also been multiplied by $\alpha(\Gamma_y)$. $r_{v,s}^{\infty}$ and $dv_{\rm fr}/dr^{\infty}$ all exhibit reasonably smooth dependences on ψ. Another indication that these fronts are all the same state is that all the experiments reveal a very low wave number. This issue is discussed in greater detail in Sec V. Finally, in Ref. [24], I suggested that the common value of the TW phase velocity measured at r_v for both $\psi=-0.408$ and -0.240 might have some significance. As seen in the last column of Table I, however, a different phase velocity is measured at r_v in the annulus. But the effect of the cell width on this measurement is quite uncertain.

IV. PRODUCTION, CHARACTERIZATION, AND MANIPULATION OF SOURCES AND SINKS

The source-front state discussed above can be transformed into a stable state consisting of a source and a sink on opposite sides of the cell. Since $v_{\rm fr}>0$ for $r>r_v$, it would seem that the fronts can be pushed together to make a sink simply by raising the Rayleigh number. However, there are several problems with this notion. First, fronts are observed to repel each other. This is not surprising, given the fact that "forwards-facing" TW pulses repel one another under essentially identical conditions [22]. Because of this, forcing fronts to merge in a reasonable time would require increasing the Rayleigh number above the value r^* at which the TW frequency drops to zero [3], and this would turn the resulting pattern into a spatially uniform state of stationary convection. A more subtle problem is revealed in Fig. 24 below: Even below r^* (in fact, even below the range of Rayleigh numbers in Fig. 4), sources and sinks tend to drift together and merge, forming a defect-free TW state.

These problems and their cure are illustrated in Fig. 5. Initially, a source-front state was created using the same procedure as in Fig. 1. At the beginning of the run in Fig. 5, the Rayleigh number was set somewhat above r_v and was spatially uniform. This caused the opposing fronts to approach each other initially; however, they repelled each other and came to a stop instead of merging into a sink (times 2000—6000 sec in Fig. 5). The Rayleigh number was then decreased below r_v (times 6000–8000 sec), and the fronts receded. Finally, a large bump centered between the two fronts was added to the spatial Rayleigh-number profile, and this caused the fronts to approach each other again and to merge without destroying the source defect on the opposite side of the cell. For a brief period after the merging of the opposing fronts (times 10 000–12 000 sec), the sink thus formed consisted of a narrow spatial region of steady

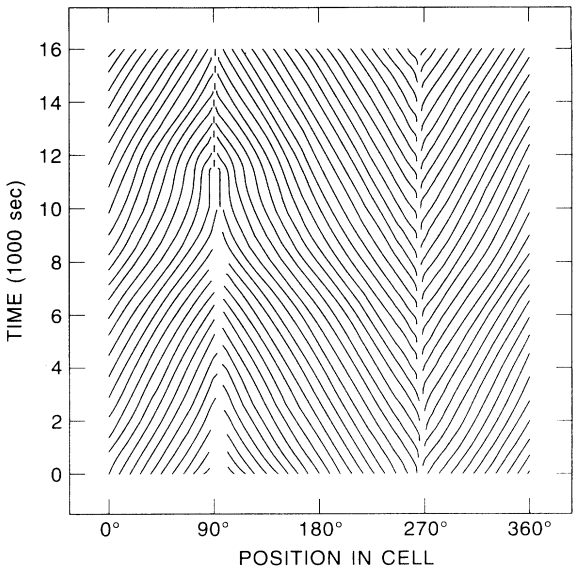

FIG. 5. Creation of a source-sink state. This run began like the run in Fig. 1 and resulted in a source-front state. Then, the Rayleigh number was increased well above r_v, causing the neutrally stable fronts to approach each other. Because of the repulsion of the fronts, a sink could be created without destroying the source only by applying local heating in the vicinity of the fronts. At the end of the run, the system was in a stable source-sink state at $r=1.249\,80$.

convective rolls. It then evolved into a true sink of TW. As shown in Fig. 6, this source-sink state can be stable for arbitrarily long times.

The stationary source-sink state shown in Fig. 6 is actually something of an anomaly. Typically, source defects tend to drift at constant velocity, and sinks tend to follow. Figure 7 shows the fastest-drifting defect pair that I have observed. Drifting defects do not appear to slow down, even on time scales of a week. Making the defects stand still is actually the challenge here, and I

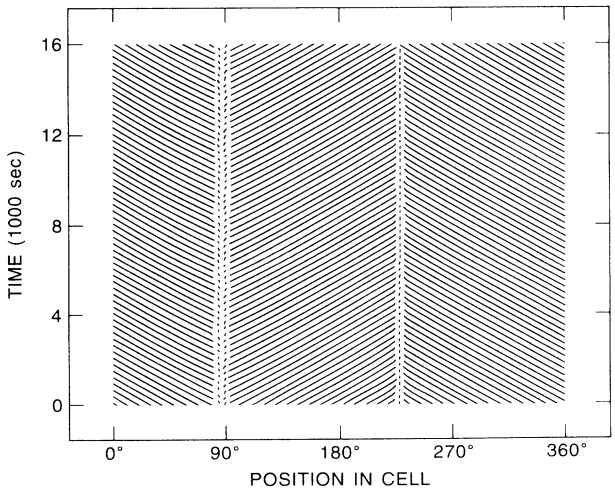

FIG. 6. A stable state consisting of motionless source and sink defects approximately opposite one another in the cell. The Rayleigh number is $r=1.234\,10$.

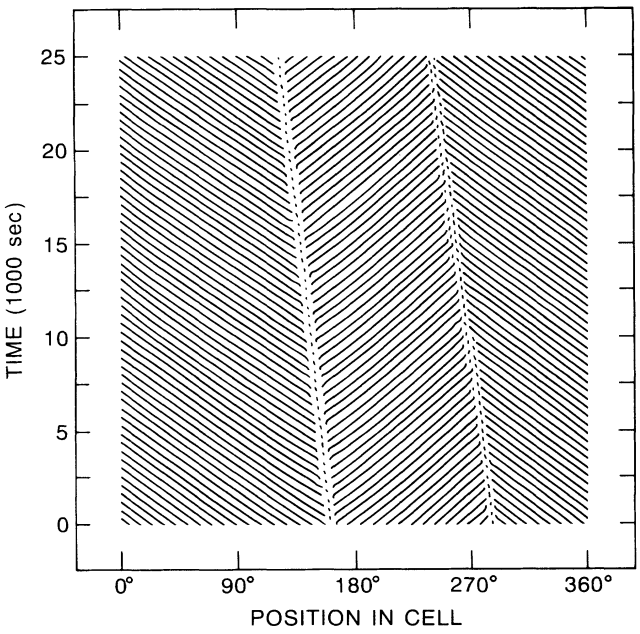

FIG. 7. A drifting source-sink state at $r=1.243\,35$. Both defects drift to the left at $v_s=-0.019\,58$.

demonstrate techniques which can used for this in Figs. 11 and 12 below. As detailed in Sec. V, the source position $x_{\text{source}}(t)$ is identified as the point where the left and right TW amplitudes are equal. In all case, $x_{\text{source}}(t)$ is observed to drift linearly in time; for this run, $dx_{\text{source}}/dt=-0.019\,471(4)$. I have found it more reliable to use the fit procedure in the next paragraphs to determine the source velocity, which I quote for this run as $v_s=-0.019\,58$. In this example, the source and the sink are so close that it cannot be assumed that they are not interacting, and I have excluded such data from the quantitative analysis described in Sec. V.

Because sources and sinks drift, two numbers, the Rayleigh number and the source velocity, must be quoted to parametrize such states. Because the oscillation frequency is monotonically related to the Rayleigh number, and because it is my impression that the frequency (or TW phase velocity) is more directly relevant to the defect structure than the Rayleigh number, I will actually speak more in terms of the frequency than the Rayleigh number in describing source-sink states. Because the oscillation frequency depends on position, it is necessary to refer to a spatially averaged frequency $\bar{\omega}$.

Figure 8 shows examples of the amplitude, wave-number, and oscillation-frequency profiles for three drifting-defect states. Several features are evident in these profiles and are worth discussing on a qualitative level before they are investigated in quantitative detail below. First, if the source and sink are not too close together [excluding Figs. 8(a)–8(c)], the amplitude profiles near the source exhibit the same rapid rise, followed by a near saturation, that was observed in the source-front states. At the sink, both amplitudes decay again. At high source velocities [Fig. 8(a)], the sink tends to follow the source rather closely, and this tends to distort the amplitude profile in the narrower space between them. Apart from this, the amplitude profiles of the defects exhibit approximate mirror symmetry. Second, judging from the amplitude profiles, the source is slightly wider at high oscillation frequency [Fig. 8(d)] than at low frequency [Fig. 8(g)], and sources are always wider than sinks. This makes intuitive sense and conforms to the description given by Coullet *et al.* [27]. Third, the wave number in all three examples in Fig. 8 is much higher at the sink than at the source. Typically, $k_{\text{source}}\sim 2.7$ and $k_{\text{sink}}\sim 3.3$. At low oscillation frequency [Fig. 8(h)], the wave-number profile interpolates almost linearly between these two values. In contrast [Fig. 8(e)], the wave-number gradient is concentrated in the near vicinity of the defects at high oscillation frequency. Outside these defect cores, the wave-number profile is flat at high frequency. Finally [Figs. 8(c), 8(f), and 8(i)], the oscillation-

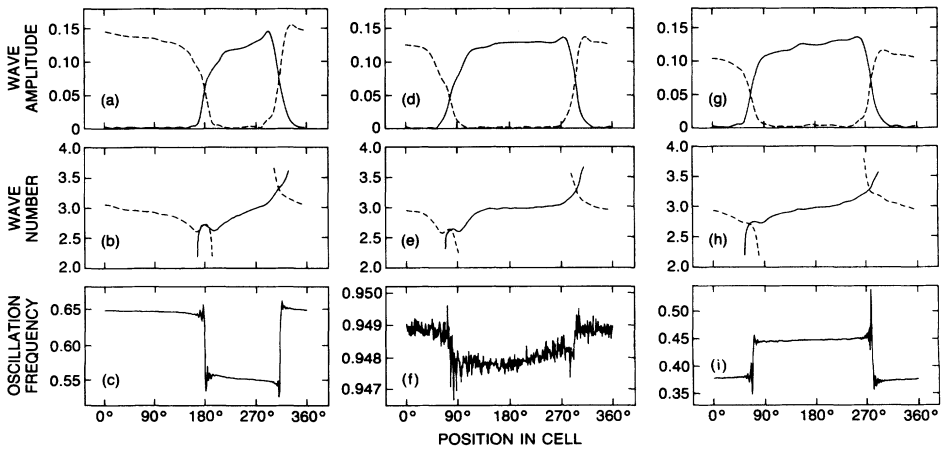

FIG. 8. Amplitude (top), wave-number (middle), and oscillation-frequency (bottom) profiles for three stable source-sink states. Left: $r=1.245\,96$, $\bar{\omega}=0.612\,04$, and $v_s=-0.016\,53$. Center: $r=1.235\,57$, $\bar{\omega}=0.984\,26$, and $v_s=-0.000\,16$. Bottom: $r=1.254\,00$, $\bar{\omega}=0.417\,54$, and $v_s=+0.01223$.

frequency profile depends strongly on the source velocity.

The spatial profile of the oscillation frequency is accurately explained as a Doppler shift. In Fig. 9, the solid curve is the frequency profile for one drifting-defect state, and the dots show a fit to the form $\omega(x)=\bar{\omega}-v_{\text{Doppler}}k(x)$, where $\bar{\omega}$ and v_{Doppler} are adjustable parameters, and the measured wave-number profiles are used to form $k(x)$:$k(x)=k_R(x)$ on the right of the source, and $k(x)=-k_L(x)$ on the left of the source. The fit is excellent in this and all other cases. Further, as shown in Fig. 10, the fit parameter v_{Doppler} exactly matches the temporal derivative of the source position $x_{\text{source}}(t)$ determined by following the point where the left- and right-wave amplitudes are equal. I think that the Doppler-shift fit gives a more reliable estimate of the source velocity than following $x_{\text{source}}(t)$ in spacetime. The spacetime method relies explicitly on accurate amplitude profiles in the vicinity of the source, precisely where the demodulation technique is affected most by noise, filter bandwidth, and cross-channel leakage (defined and discussed below). The Doppler-shift fit is much less sensitive to the accuracy of the demodulation; the data near the defects are excluded from these fits anyway, since the oscillation-frequency profiles exhibit hard-to-fit interference beats there. Thus, I identify the two fit parameters v_{Doppler} and $\bar{\omega}$ as the source velocity and the spatially averaged oscillation frequency, respectively, and these numbers are precise to at least three and four digits, respectively.

Because source defects exhibit a Doppler shift, and because the TW frequency depends on Rayleigh-number, local heating can be used to manipulate sources. Making the Rayleigh number higher on one side of a source than on the other causes a frequency difference between the two TW components, and the source adjusts its velocity so that the Doppler shift matches this frequency difference. This observation can be summarized by the statement that hot spots repel sources. Figure 11 illustrates this effect. The defect state under observation in this figure is the same run as in Fig. 7. At the beginning of this run, the Rayleigh number was set at $r=1.243\,35$, and the spatial profile of the Rayleigh number, as measured using the drifting-pulse technique described in Ref. [22], had the nearly flat shape shown as the curve marked (1) in Fig. 11(b). At time $t=12\,600$ sec, a local heat source was applied at location 158°, producing the Rayleigh-number profile marked (2). The source responded by drifting faster to the left, away from the local bump in the Rayleigh-number profile, as can be seen in the time period marked (2) in Fig. 11(a). At later times, in order to follow the drift of the source, the bump was moved further and further to the left, as illustrated by the curves marked (3) and (4) in Fig. 11(b). Interestingly, the sink defect was hardly affected by the manipulations of the source. On the basis of this and other observations (for example, see Fig. 23 and discussion below), I conclude that the sink defects are "passive" and merely tend to follow the sources. The observation that unperturbed defects drift at constant velocity for long periods is further confirmation that the cell is extremely uniform. In a nonuniform cell, sources would get stuck at local minima in the Rayleigh-number profile.

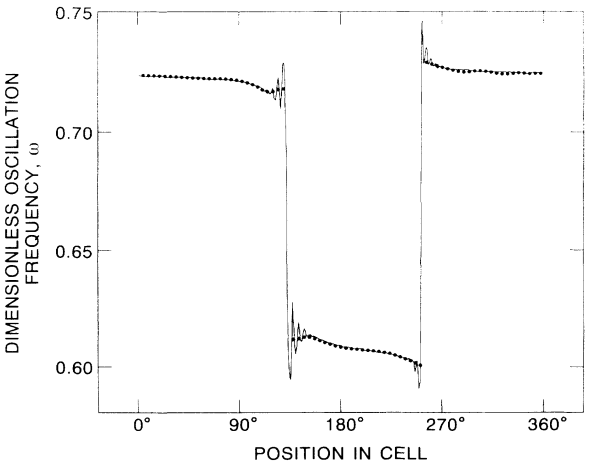

FIG. 9. The solid curve is the oscillation-frequency profile for a source-sink state at $r=1.243\,35$. The dots show the fit to the Doppler-shift form quoted in the text. For this example, the fit parameters are $v_{\text{Doppler}}=-0.019\,58$ and $\bar{\omega}=0.671\,06$. The regions near the defects, were interference beats are seen, are excluded from the fit.

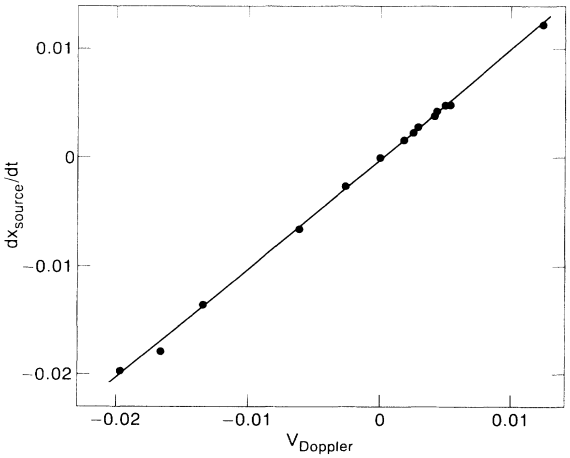

FIG. 10. The source velocity dx_{source}/dt determined by following the source position in spacetime is plotted against the Doppler-shift velocity v_{Doppler} determined by fits of the type illustrated in Fig. 9, for a subset of the data files analyzed. The line is a least-squares fit with slope 0.996 ± 0.006. The average difference between these two velocities, including all the data, is $(0\pm2)\times10^{-7}$.

Figure 12 illustrates the use of these techniques on a source-front state. Initially, $r=1.259\,02$, and the Rayleigh-number profile was quite flat (dashed curve in bottom frame of Fig. 12). Since $r\sim r_v$, the fronts as well as the source were essentially stationary. At approximately $t=6000$ sec, local heating was applied at location 53°, producing the full Rayleigh-number profile in the lower frame of Fig. 12. Since the left-hand front in the top frame is found near the location in the apparatus where the applied temperature difference is held constant by the temperature-regulation system, this front was affected very little by the local heating. Closer analysis of

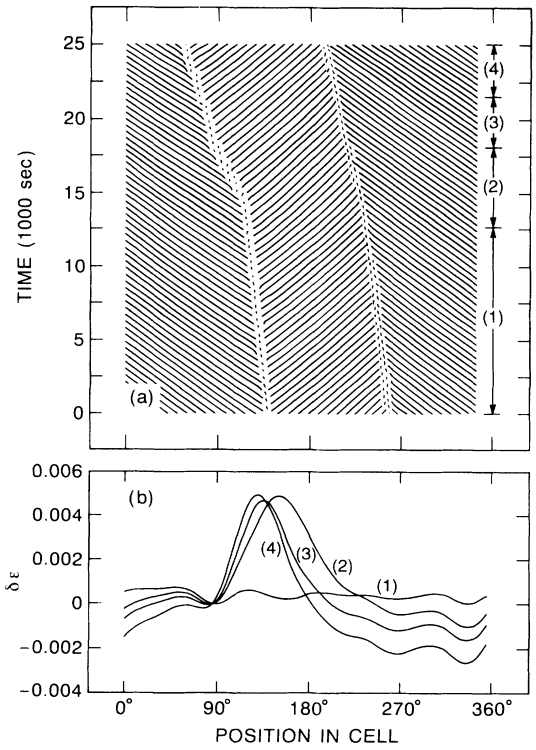

FIG. 11. Manipulation of a source defect by local bumps in the Rayleigh-number profile. Part (a) shows the spacetime trajectories of the roll boundaries, and the curves in part (b) show the reduced Rayleigh number profile $\delta\epsilon(x)=[r(x)-\bar{r}]/\bar{r}$, where $r(x)$ is the applied Rayleigh-number profile and $\bar{r}$ is the reduced Rayleigh number measured with no local heating. Initially, the Rayleigh number exhibited the flat profile shown as the curve marked (1) in part (b), and the source and sink defects drifted to the left [time period (1) in part (a)]. In the time periods marked (2), (3), and (4) in part (a), the correspondingly labeled Rayleigh-number profiles in part (b) were imposed by turning on point heaters on the underside of the cell. The Rayleigh-number gradient applied across the source enhanced the frequency difference between the left and right TW, and the source velocity increased so as to impose a corresponding increase in the Doppler shift.

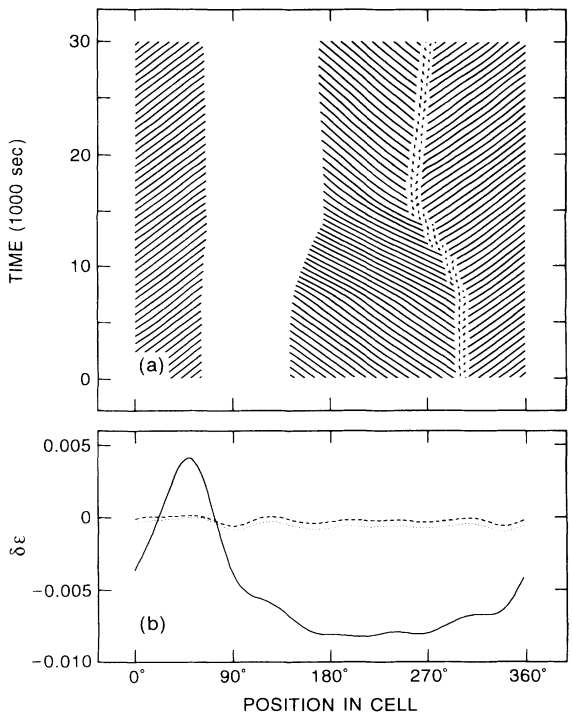

FIG. 12. Manipulation of a source-front state by local heating. Between times 0 and 6000 sec, the flat, dashed Rayleigh-number profile in (b) was applied, and the fronts and source were all stationary. Between times 6000 and 15 000 sec, a Rayleigh-number profile of the form of the solid curve in (b) was applied, and the source and one of the fronts moved accordingly. Finally, the flat, dotted Rayleigh-number profile was restored, and the defect motion stopped again.

the left-hand front behavior indicates that the front responds to the Rayleigh number measured ahead of its half-amplitude point by a distance of approximately 3.5 times the cell height, in agreement with the response of drifting pulses [22] and spatially uniform TW [3] to Rayleigh-number nonuniformities. The right-hand front, finding itself in region where $r<r_v$, receded during the time period that the Rayleigh-number bump was applied [28]. As in Fig. 11, the source defect, initially at location 300°, was strongly repelled by the Rayleigh-number bump. At $t=14\,000$ sec, a flat Rayleigh-number profile was restored [dotted curve in Fig. 12(b)], and the defect motion stopped.

V. QUANTITATIVE MEASUREMENTS OF DEFECT STRUCTURE

In this section, I describe the methods used to analyze defect structure using profile measurements like the ones presented in Figs. 2 and 8. I illustrate the techniques used by describing the analysis of the source wave-number profile in the source-sink state in detail. I then discuss the results obtained for the rest of the defects observed, starting with the source-sink state and finishing with the source-front state. Except as noted, all amplitude and wave number profiles were analyzed in the same way.

I have defined the location of sources and sinks as the point where the left- and right-TW amplitude profiles are equal. I have also verified that computing the average of the positions at which the slopes of the two profiles are steepest gives essentially identical results. Front locations were determined differently, as discussed below. With the defect positions thus determined, I then shifted all the profiles to a standard mesh of distances from the defect center which covers 60% of the experimental cell. Left-TW profiles were reversed, so that the "distance from the defect" increased from left to right for all profiles. Separate left and right files were made for each source and for each sink defect. Data near the other defect, on the far right of each profile, were removed before further analysis.

The next question to be considered is that of symmetry with respect to reflection through the center of the defect. Since sources and sinks drift, I expected to find an asym-

metry in their amplitude and/or wave-number profiles that is proportional to the drift velocity. A careful search for such an effect was performed only on the source wave-number profiles in the source-sink state. The results of this analysis depended on the oscillation frequency. At low frequency, the wave-number profiles exhibited small asymmetries far from the source. These were clearly related only to the fact noted in the discussion of Fig. 8 above that, at low oscillation frequencies, the wave number exhibits an almost linear increase from k_{source} to k_{sink} as one moves from the source to the sink. Since, in most data sets, the two defects were not exactly diametrically opposite in the cell, this causes an asymmetry. I was not able to find a relationship between this rather trivial effect and the drift velocity.

At high oscillation frequency, the situation is different. In this case, most of the wave-number gradient is concentrated in the cores of the defects, with a flat profile in the regions between the defects—this was also noted in connection with Fig. 8 above. Thus, in these data sets, the unequal source-sink distances primarily affect only the lengths of the flat-wave-number-profile regions and not the shapes of the profiles in the defect cores. Thus, any measured asymmetry in the defect cores would probably represent the intrinsic response of the defects to their drift. However, no effect greater than the noise could be identified. I suspect that this is because the drift velocities are low: The highest ratio of drift velocity to TW phase velocity of all the data was 0.08. Because the asymmetries in the profiles are so small, I averaged the left- and right-TW profiles in all the subsequent analysis, and this essentially cancels any true drift-velocity-related asymmetries in the high-oscillation-frequency wave-number profiles. The result of this averaging in the case of the asymmetric, low-oscillation-frequency source-sink states is effectively to yield profiles characteristic of source-sink states in which the defects are exactly diametrically opposite one another in the cell.

The next step in the analysis is to explicitly examine the oscillation-frequency dependence of the profile under study. Figure 13 shows the frequency dependence of the source wave number at several different distances from the defect. The data at each spatial position exhibit a scatter of about $\pm 1\%$, caused by wiggles due to optical distortions. Since the distortions move around the image in a way which is unrelated to the defect drift, this scatter is essentially random and can be averaged away. In the present case, this was done by fitting the frequency dependence at each spatial point using a heavily smoothed cubic spline, as shown by the curves in Fig. 13. In other profiles, no frequency dependence was observed, and I simply averaged all the profiles together in such cases. Because of this averaging, the source-sink wave-number profiles are accurate to much better than $\pm 1\%$, and the amplitude profiles are accurate to $\pm 1-2\%$. The source-front state profiles are somewhat less precise, as noted below.

Figure 14 shows the spatial profiles of the source wave number in the source-sink state, as interpolated to several different oscillation frequencies using the spline fits in Fig. 13. At all frequencies, the wave number is very low

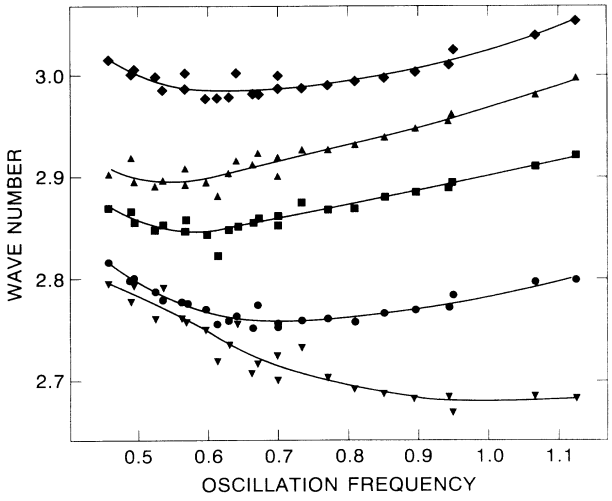

FIG. 13. The wave number measured at different distances from the source in the source-sink state is plotted as a function of oscillation frequency. From bottom to top, the distances from the source, in units of the cell height, are: inverted triangles, 1.83; circles, 6.41; squares, 8.71; triangles, 11.00; and diamonds, 15.58. The solid curves are heavily smoothed spline fits to the frequency dependences at each spatial point.

behind the source, rises to a maximum at the defect center, exhibits a sharp dip, and then rises again. (An assessment of how much of this reproducible behavior is real and how much is an artifact of the demodulation process will be postponed until the demodulated amplitude profiles are discussed below.) Beyond the initial minimum at $x/d \sim 4$, the wave-number profile for the lowest frequency increases smoothly with distance from the source, as previously mentioned. The "core" region, over which the wave-number gradient is concentrated,

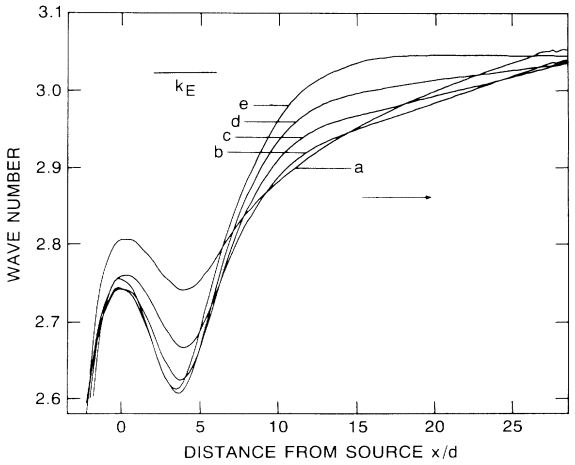

FIG. 14. Wave-number profiles near the source defect in the source-sink state are shown for different oscillation frequencies, as interpolated using the spline fits shown in Fig. 13. Curves $a-e$ are for frequencies 0.50, 0.65, 0.80, 0.95, and 1.10, respectively. The horizontal bar labeled k_E represents the center of the Eckhaus boundary found in I. In this and subsequent figures, the arrow shows the direction of TW propagation.

shrinks in space as the frequency increases, so that, for the highest frequency in Fig. 14, the half-width of the defect core is about 12 times the cell height. Figure 15 shows the sink-wave-number profiles for the source-sink state, interpolated to slightly different frequencies than in Fig. 14. Once again, the extent of the core region shrinks as frequency increases. Because the averaging described above effectively produces the wave-number profiles for a state of diametrically opposite defects, the wave numbers at corresponding frequencies in Figs. 14 and 15 are seen to match at a distance $x/d=20.62$, which corresponds to $\frac{1}{4}$ of the cell circumference.

It can be read from Fig. 14 that, at the highest frequencies, the TW outside the core regions of the defects exhibit a flat wave-number profile with $k=3.045$. This coincides almost exactly with the wave number $k_{40}=3.0474$ of the $n=40$ spatially uniform TW state discussed in I. As shown in Fig. 16, the oscillation frequencies of these two states also coincide at the low Rayleigh numbers which correspond to the highest frequencies. My interpretation of these observations is that, at high-oscillation-frequency, source-sink states consist of localized defects which are separated by wide regions in which the TW state is identical to the spatially uniform TW studied in I. The wave number in these regions lies near the center of the Eckhaus boundary (see Fig. 20 below), and it is thus very tempting to conclude that it is selected by the Eckhaus instability rather than the source. At low oscillation frequency, the defect cores extend throughout the system, and the Eckhaus instability is clearly not relevant. These observations also suggest that the Rayleigh-number dependence of the source-sink-state frequency depends on the cell size. The defect-state oscillation frequency coincides with the uniform-state frequency for frequencies above which the core size is sufficiently small compared to the cell size. In a larger cell, the Rayleigh-number range over which these two frequencies are equal would extend to higher values.

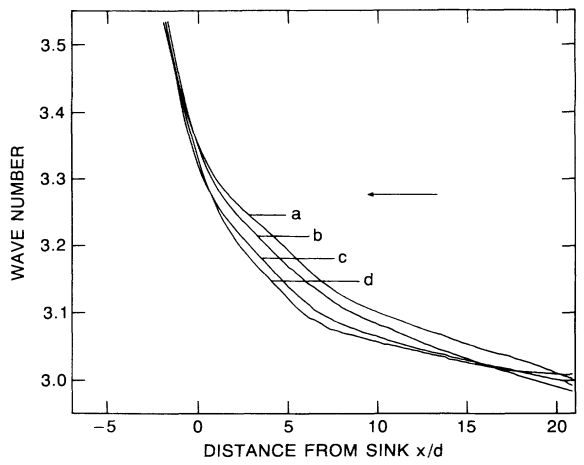

FIG. 15. Wave-number profiles near the sink defect in the source-sink state are shown for different oscillation frequencies, as interpolated from spline fits to the frequency dependence at separate spatial points. Because of peculiarities of the data, interpolation was made to a different set of frequencies than in Fig. 14. Curves $a-d$ are for frequencies 0.48, 0.63, 0.78, and 0.93, respectively.

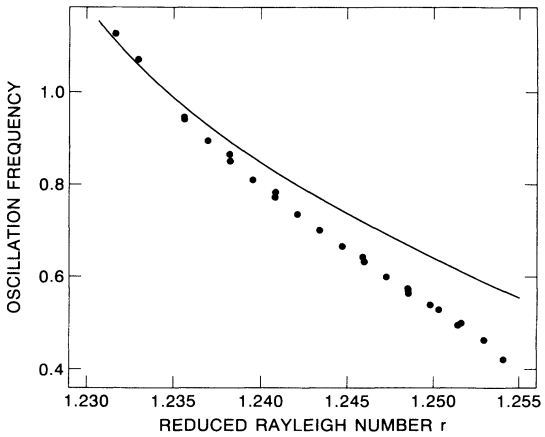

FIG. 16. The symbols represent the Rayleigh-number dependence of the source-sink-state oscillation frequency $\bar{\omega}$, as extracted from fits like the one in Fig. 9. For comparison, the solid curve shows the oscillation frequency of the spatially uniform $n=40$ state measured in I. Below $r\sim 1.234$, the defect cores fill only a small fraction of the system, and the defect-state frequency matches the uniform-state frequency.

The amplitude profiles of the source-sink states are analyzed in the same manner as the wave-number profiles, with one difference. The amplitude profiles typically do not saturate completely as one moves further and further from the source. Instead, as can be seen in Fig. 8(d), the amplitude continues to grow, albeit slowly, until it drops abruptly at the sink. To compensate for the fact that the source-sink distance is not the same for all data sets, I normalize each amplitude profile to its value averaged over some small domain far from the source before searching for a frequency dependence.

As shown in Fig. 17, the source amplitude profile depends on oscillation frequency. Moving downstream from behind the source, the amplitude initially grows abruptly, with a slope that decreases with frequency, and then reaches a frequency-dependent plateau before continuing to grow downstream. The dashed line in Fig. 17, taken from low-frequency data in the source-front state, appears to match this trend. Intuitively, one would expect that, as the TW leave the source at higher velocity, the initial rise in the amplitude profile would be stretched out, and this is confirmed by these data. By contrast, as shown in Fig. 18, the amplitude profile of the sink is independent of frequency. This profile exhibits a (10–90)% width of 3.8 times the cell height, which is quite a bit sharper than even the sharpest source profile (shown for reference in Fig. 18 as the dashed curve).

It is useful at this point to consider some of the artifactual features of the demodulation process and how they affect these amplitude and wave-number profiles. The main artifact in this process comes from what I call "cross-channel leakage." Behind the source and ahead of the sink, the opposite TW component is present at 100% amplitude and cannot be completely removed by the demodulation. My experience is that this stray signal is attenuated only by a factor of about 100 by the demodu-

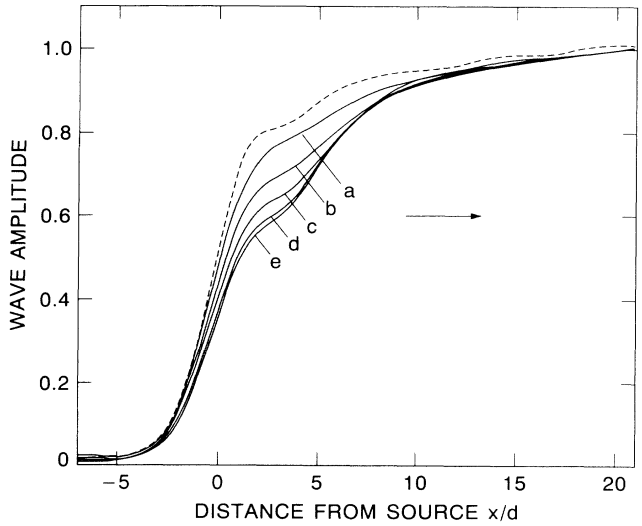

FIG. 17. The solid curves show the amplitude profiles near the source defect in the source-sink state for different oscillation frequencies. Each individual profile used in this interpolation was normalized so that its amplitude, averaged over a domain centered at $x/d=22.7$, is unity. Curves $a-e$ represent frequencies 0.50, 0.65, 0.80, 0.95, and 1.10, as in Fig. 14. The dashed curve shows the average of the amplitude profiles in the source-front state. In that state, the oscillation frequency was 0.48 ± 0.06. A consistent broadening of the profile with increasing frequency is seen.

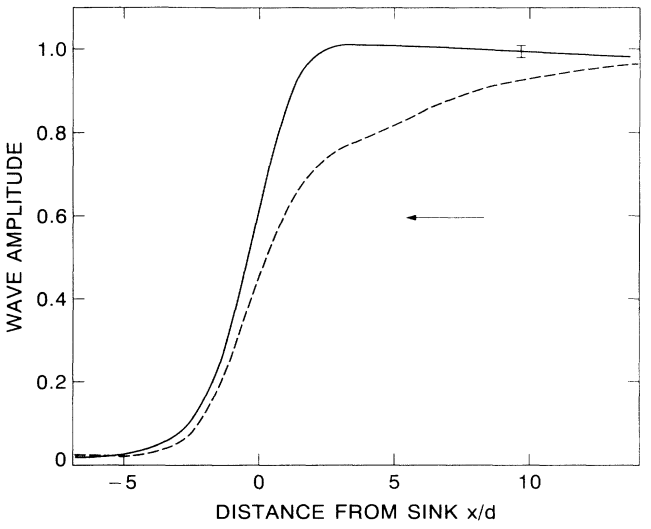

FIG. 18. The solid curve shows the amplitude profile near the sink defect in the source-sink state. Each individual profile used in this average was normalized so that its amplitude, averaged over a domain centered at $x/d=10$, is unity. The error bar shows the standard deviation of those individual amplitude profiles. The averaged profile is sharper than the sharpest source-amplitude profile (dashed curve, copied from the dashed curve in Fig. 17). Note that the TW are still growing in amplitude as they reach the sink.

lator filters, using typical filter settings. Thus, leakage of the opposite TW component is an important component of the profiles in Figs. 17 and 18 for $x/d \lesssim -3$ and is dominant for $x/d \lesssim -5$. It is for this reason that the TW amplitude profiles decay only to 1% levels far behind the defects in Figs. 17 and 18. In contrast, there is no oppositely propagating TW component beyond the front profile in Fig. 21 below, and its amplitude drops all the way to zero. A rough correction for this "cross-channel leakage" could be made in the case of the source-sink state by computing the profile $A'(x)=A(x)-\alpha A(-x)$, where $\alpha\sim0.01$ is adjusted so that the amplitude drops to zero far behind the defect. This correction causes a negligible change in the (10–90)% width.

The spatial domains over which the wave-number profiles in Figs. 14 and 15 have been plotted do not include the regions where this cross-channel leakage distorts the amplitude profiles. However, the sharp spatial variations of the wave-number and amplitude profiles also might cause other distortions of the wave-number profiles. Experiments with artificial data reported in Ref. [19] found that sharp amplitude variations do not affect the wave-number profiles, and my experience since has been that wave-number profiles are distorted only at too-narrow demodulator bandwidth, and even then only in spatial regions where the signal is strongly attenuated. Further, experiments with artificial data that match these source-sink states suggest that, with the exception of the part of the wave-number profile behind the source where $k<2.65$, all of the behavior in Fig. 14 is real. All of the sharp rise in the profiles in Fig. 15 seems to be real behavior too.

The noise and distortions in the amplitude and wave-number profiles computed for the source-sink state have been substantially reduced by averaging. This improvement has been less successful in the case of source-front states because they do not tend to drift in the cell. Since all the source-front data were acquired in a single three-day period, the wiggles caused by optical distortions in the data were also basically stationary. Thus, averaging reduced noise but not distortions.

The amplitude profile near the source in the source-front state has already been displayed in Fig. 17. Figure 19 shows the wave-number profile near the source in this state, interpolated to four different oscillation frequencies. (Note that the frequencies in these data lie in a narrow range which is close to the lowest frequency in Fig. 14.) The rise and dip very close to the defect center have the same appearance as the front profiles in Fig. 14. In this state, however, beyond about $x/d\sim10$, the wave-number profiles flatten out at all frequencies, never exceeding a value of about 2.9. This wave number is low not only in comparison with the source-sink-state wave number; it is also low with respect to the Eckhaus boundary measured in I. This is shown in Fig. 20, where the left and right ends of the horizontal arrows marked $a-d$ represent the wave numbers measured at positions $x/d=10$ and 27, respectively, in the corresponding profiles in Fig. 19. The wave number at the center of the source lies well outside the Eckhaus boundary for all the defect states studied in this work. In the source-front

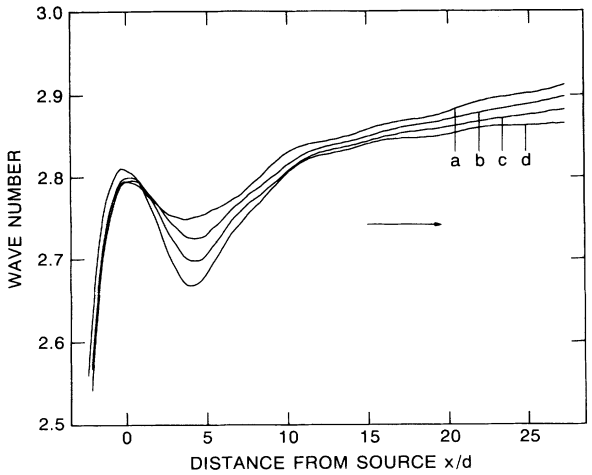

FIG. 19. Wave-number profiles near the source defect in the source-front state are shown for different oscillation frequencies. Curves $a-d$ are interpolations to frequencies 0.40, 0.45, 0.50, and 0.55, respectively. Unlike the profiles in the source-sink state, these wave numbers remain low even far from the source.

states at the lowest Rayleigh numbers, much of the rest of the wave-number profile is also outside the Eckhaus boundary.

Finally, Fig. 21 shows the spatial profile of the TW amplitude near the front in a source-front state. This amplitude profile was found to exhibit no frequency dependence over the rather narrow frequency range of the data. The location $x/d=0$ was defined as the 50% amplitude point in the right-TW front for each data set, and the

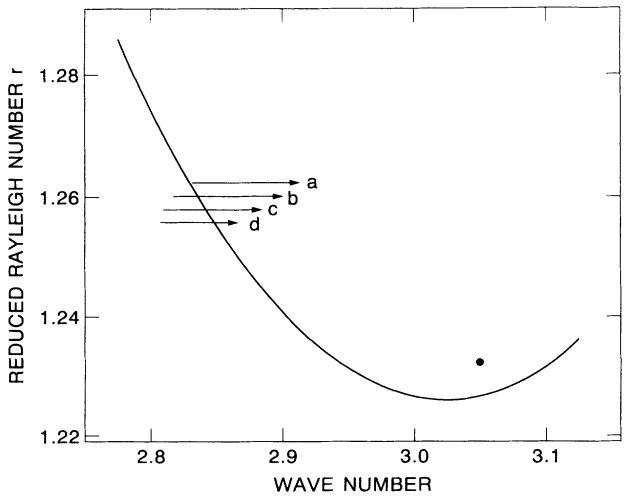

FIG. 20. The arrows marked $a-d$ illustrate the behavior of the corresponding wave-number profiles in Fig. 19 as one moves from point $x/d=10$ in the wave-number profile (tail of arrow) to point $x/d=27$ (head of arrow). The curve is the parabolic fit to the Eckhaus boundary found in I, and the solid circle represents the wave number in the flat part of the $\bar{\omega}=1.10$ profile in Fig. 14. The wave number at the source always lies outside the Eckhaus boundary, and much of the rest of the wave-number profile in the source-front states is also outside this boundary.

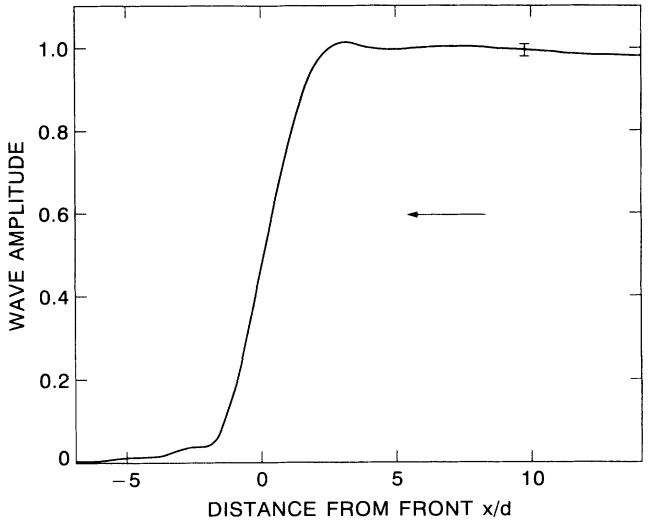

FIG. 21. The average amplitude profile near the front in a source-front state is shown. Moving downstream from the right, the TW continue to grow weakly until the amplitude drops sharply at the front. Beyond the main drop in amplitude, there is a small shoulder, and then the amplitude decays entirely. The profile appears to be fully resolved and unaffected by leakage through the demodulator filters.

profile of the opposite TW component was reversed and shifted until the best overlap with the right-wave profile was found. The profile in Fig. 21 is just the average of all the left- and right-TW amplitude profiles, once again normalized to the amplitude averaged over a spatial domain far from the front. The drop in amplitude at the front is quite sharp: The (10–90)% width is 3.0 times the cell height. Far beyond the front, because there is no cross-channel leakage in the demodulation in this state, the wave amplitude drops to zero. The narrow shoulder structure seen for $-6\lesssim x/d\lesssim -2$ appears to be real.

VI. QUALITATIVE OBSERVATIONS OF DEFECT BEHAVIOR

I conclude the descriptive part of this paper with a few final qualitative observations of defect structure and evolution. While the structure of the amplitude and wave-number profiles have been well documented in the previous section, it is also worth considering how the actual convective rolls behave in defects. This is the subject of Fig. 22. In the upper left of this figure, raw spatial shadowgraph signals spanning a time range of a bit less than half an oscillation cycle are shown for a source defect. During this time period, an adjacent minimum and maximum in the center of the graph are pulled apart, giving birth to a new pair of extrema in between the original two. Since the extrema of the shadowgraph signals represent roll boundaries, this evolution represents a single convective roll that first expands in width and then splits in three. A sketch of this process is shown in the lower left part of Fig. 22. The evolution of a sink defect, shown in the upper right part of the figure, is different. Here, two adjacent minima in the center of the pattern

are compressed and merge as the maximum between them disappears. As sketched in the lower right of the figure, this corresponds to the compression and disappearance of an adjacent pair of convective rolls. There is a fundamental asymmetry between the microscopic structure of source and sink defects.

This asymmetry is also seen in the response of the defects to external perturbations. This is illustrated in Fig. 23. During the beginning of this run, the temperature regulation system malfunctioned, causing the Rayleigh number to fluctuate wildly. As this problem was being examined and repaired in the middle of the run, the Rayleigh number was changed deliberately, for diagnostic purposes. Finally, the apparatus settled down to a well-regulated state. During all these changes, the spatial profile of the Rayleigh number in the cell was uniform. Nonetheless, the source defect broke up erratically, while

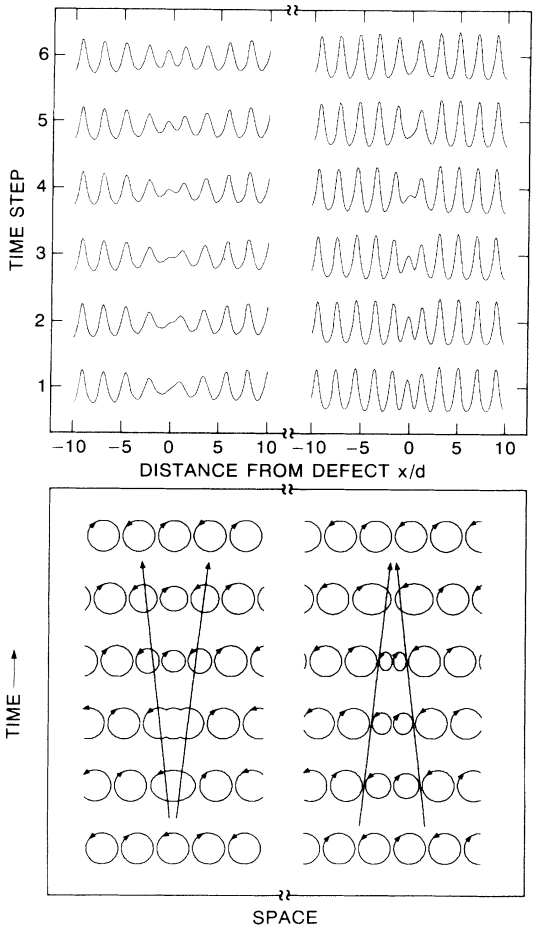

FIG. 22. Top: Raw shadowgraph signals which cover spatial regions centered on a source defect (left) and a sink defect (right). The time period spanned is somewhat less than half of the oscillation period. Bottom: The circulation in the convective rolls, as viewed along the roll axes, is sketched in correspondence with the shadowgraph signals. In these sketches, the time period scanned is exactly one-half of an oscillation period. The source is formed by a single roll which stretches out and splits into three. The sink is formed by a pair of rolls which shrink and disappear. In this run, the shadowgraph system was operated in a slightly nonlinear regime, giving the signals a slightly nonsinusoidal shape.

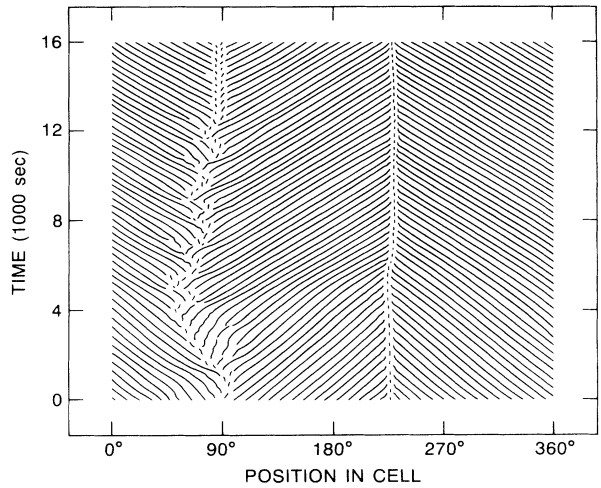

FIG. 23. Behavior of a source-sink state during a period of strong fluctuations of the Rayleigh number. Initially, the Rayleigh number exhibited erratic fluctuations about $r \sim 1.241$ because of a loose connection in the temperature-regulation system. These fluctuations seem to have destabilized the source defect without affecting the sink. Temperature stability was regained at about time 9600 sec, and this caused the source to become state and motionless again.

the sink defect was only slightly perturbed. After the Rayleigh number settled back down at the end of the run, the source defect restabilized. In this state, the source defect imposes the wave number, determines the Doppler shift, and responds to perturbations, in ways that are sensitive to the system parameters. The sink appears to be passive.

The final qualitative issue concerns the behavior of the source-sink state at the Rayleigh-number limits of its existence. As the Rayleigh number is increased, the oscillation frequency decreases, as shown in Fig. 16. However, as shown in Fig. 24, the source and sink defects lose sta-

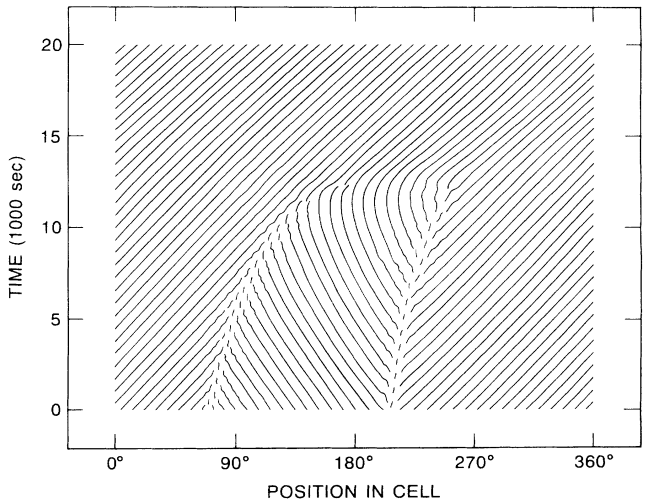

FIG. 24. Decay of a source-sink state at high Rayleigh number. This run began 10 min after the Rayleigh number was increased from 1.252 95 to 1.254 33. The decay of the state began with the sink moving closer to the source. Then, the TW in the region between the defects reversed propagation direction, and the defects disappeared.

bility well before the frequency drops to zero. In this case, the defects were drifting rather rapidly, and, as noted above, the sink tends to follow the source rather closely in such a situation. In this run, the decay of the defects begin with the sink moving even closer to the source. Then, the TW in the space between simply reversed their propagation direction, and the defects disappeared. This behavior is seen only at high Rayleigh number, and the reason for this is clear from the concentration-field measurements reported in Refs. [29,30]. The propagation of the pattern in this system is caused by a roll-to-roll contrast in ethanol concentration which varies with Rayleigh number. For an individual convective roll to reverse its propagation direction as in Fig. 24, it has to exchange ethanol with its neighbors by diffusion. This diffusion is enhanced at high Rayleigh number by the more vigorous circulation of fluid inside the convection rolls.

Figure 25 illustrates the fate of the source-sink state at low Rayleigh numbers. In this case, the low-amplitude regions in the vicinity of the defects open up into quiescent regions, and these grow at the low Rayleigh number in this run, causing a transition to the conductive state everywhere the cell. Interestingly, this happens substantially above the saddle-node Rayleigh number. In this regime, as noted above, the TW between the defects appear to be identical to the spatially uniform $n=40$ TW state. Thus, after the decay of the defects, the system is in the same state locally as it was during the decay of the uniform $n=40$ TW state illustrated in Fig. 26 of I.

VII. DISCUSSION

The experiments described in this paper demonstrate how to produce, manipulate, and characterize two states of stable spatiotemporal defects: a source-front state and a source-sink state. I begin this discussion by describing other interesting defect states which have *not* been explored in this work. I have not produced or studied a sink-front state. It is not clear that such a state can be maintained in this system—see below. I have not seriously examined source-sink states which consist of larger numbers of defect pairs. A state of four defects is in fact easier to produce in this apparatus than the two-defect states described above. However, finite-size effects are already evident in the single-pair source-sink state at all but the highest frequencies, and they would certainly dominate in all source-sink states with more than one pair of defects, in a cell of the present size. In this vein, I have not explored the effect of system size—a substantially larger cell would be hard to construct. I also have not been successful at making motionless source-sink defects at the highest Rayleigh numbers. A diametrically opposite pair of motionless defects would probably persist to higher Rayleigh numbers than that in Fig. 24, in which moving, nearby defects lose stability. I have also alluded to the fact that approaching fronts seem to repel each other like the forward-facing pulses described in Ref. [22]. This suggests that front collisions could be explored just like pulse collisions. This has not been done, however. Finally, I have not made observations of defect behavior at other values of the separation ratio ψ, and it is not clear whether the behavior observed here would be duplicated in experiments with other fluids. Such experiments will be performed in the future.

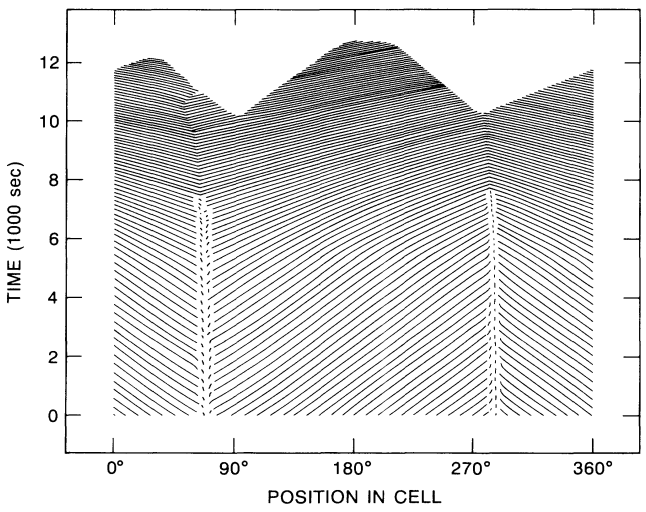

FIG. 25. Decay of a source-sink state at low Rayleigh number. This run began 5000 sec after the Rayleigh number was reduced to 1.231 59. The amplitude minima near the defects turned into true quiescent regions, which then grew to fill the cell, much like the state in Figs. 25 and 26 in I. The Rayleigh number in this state was quite a bit above the saddle-node Rayleigh number $r_s=1.226\,43$.

There is some overlap between the results described in this paper and previous observations of spatiotemporal defects in TW systems. Joets and Ribotta observed motionless sources in experiments on convection in liquid-crystal layers [12]. They also observed states in which unidirectional TW reversed direction, sometimes instantaneously. They referred to the latter case as "twin boundaries." These observations can be characterized as source defects in which the source moves faster than the TW phase velocity. In the case of "twin boundaries," the source velocity is infinite. By contrast, in the present work, the source velocity is always much slower than the TW phase velocity, and it is my intuition that this must always be so in this system. Joets and Ribotta also saw "shocks": spatiotemporal dislocations which appear periodically in a unidirectional TW state. Such defects are not seen here. Finally, the merging of a source and sink, as in Fig. 24, was reported by Couder *et al.* [13].

Spatiotemporal defects in TW convection in binary fluids in an annulus were also a dominant subject in the work of Bensimon *et al.* [11]. There, however, we mostly described the role of random arrays of dislocations in spacetime in the transient process by which complex TW states "anneal" into unidirectional TW. We were unable to stabilize a stable source-sink state; indeed, we could only stabilize a source defect by inserting a wall in the cell to serve as the sink. In both experiments, source defects have been found to be delicate and to drift. Bensimon *et al.* were able to see one defect state that I have not seen in the present experiments: a sink-front state. However, this state was not quite stable. The TW frequency was anomalous, and the fronts receded slowly and

ultimately lost stability. The double-forward-facing pulses observed in Ref. [22] could be described as a sink-front state of fixed length. However, it is unclear whether a truly stable sink-front state of arbitrary length can be made in this system.

The present experiments have shown that source defects can drift without deceleration. Because of this drift, the emitted TW exhibit a Doppler-shifted frequency. Because the frequency also depends on Rayleigh number, local heating can be used to push sources around. The sink defects, on the other hand, appear to behave passively, typically drifting along with the sources. The observation of beats in the oscillation-frequency profiles near source and sink defects is a clear indication, independent of the results of complex demodulation, that the cores of these defects consist of oppositely propagating TW with comparable amplitudes and slightly different frequencies.

The amplitude and wave-number profiles in the vicinity of the source defect are similar in the source-sink state and the source-front state. The source wave number is low, $k_{\text{source}} \sim 2.7$, and the amplitude grows from zero to a nearly saturated value in a spatial domain whose size increases with increasing TW frequency. In the source-front state, the wave number remains low downstream and is apparently selected by the source. In the source-sink state, the wave number increases downstream to a value $k_{\text{sin}} \sim 3.3$ at the sink on the other side of the cell. In one sense, this increase in wave number is not surprising: as TW approach a sink, they are compressed. However, this compression does not seem to happen in the source-front state. In considering this apparent difference between the two states, it should be remembered that source-front states have only been studied at much higher Rayleigh number than the source-sink states because the fronts would recede too fast at the lower Rayleigh numbers. Thus, the profiles in the two states are not directly comparable. In a very much larger cell, high-frequency source-front states could be studied for long times before the motion of the front emptied the cell. The interesting question that could be resolved by such experiments is whether the wave number grows to large values far from the core of the source defect in high-frequency source-front states.

The wave-number profile in the source-sink state depends strongly on frequency. At low frequency, the wave-number profile consists of a smooth interpolation between the values at the defects. At higher frequency, the wave-number gradient is concentrated in core regions of decreasing size, which are separated by regions of uniform wave number. This shrinking of the core of the source wave-number profile as the frequency increases is a bit counterintuitive. One might expect that, with increasing TW velocity, the source wave-number profile would be stretched out in space, like the amplitude profile, rather than compressed. In the uniform-wave-number regions observed at high frequency, the wave number and frequency are the same as in the $n=40$ spatially uniform state. The fact that this state lies in the center of the Eckhaus band makes it tempting to conclude that the Eckhaus instability selects this state, despite the role of the source in the selection that is clearly seen in the source-front state. This is discussed further below.

Interestingly, the downstream increase in local wave number observed in the defect states in this paper is exactly the opposite of the trend seen in pulses [22] at this separation ratio and in confined states of arbitrary length seen at more negative separation ratio [31]. In those states, $k(x)$ is high at the trailing edge and drops to a low value at the front of the confined state. The increase in the local wave number near the front in the source-front state studied here is especially puzzling, since it appears that this front is stabilized by the same microscopic mechanism as the leading-edge fronts in the earlier confined states [30, 32].

The comparative shapes of the amplitude profiles of the different defects can be summarized by the statement that sources are noticeably wider than sinks, which in turn are slightly wider than fronts. Sources grow wider with increasing frequency, while the amplitude profiles of sinks and fronts appear to be independent of frequency over the narrow frequency ranges in which they can be studied. The (10–90)% width over which the TW amplitude decays in sinks and fronts, $3.0d$ to $3.8d$, is similar in magnitude to the distance downstream at which pulses, fronts, and uniform TW respond to Rayleigh-number nonuniformities—$3.5d$ to $4.7d$. The relationship between these two similar lengths is unclear.

A comparison of the source-front states described herein and the neutrally stable fronts studied in rectangular cells [24] leads to the conclusion that they are the same state. In Ref. [24], I also showed that the TW behind the front in a rectangle have the same frequency and wave number as TW which fill the cell. This implies that the Eckhaus instability plays no role in TW convection in a rectangular cell, because the wave number is selected by the source, which in this case corresponds to one of the end walls. This suggests two interesting questions which could be answered by further experiments in rectangular cells: First, how does a full-cell, unidirectional TW state decay to the conductive state at the lowest Rayleigh numbers? In an annulus, this decay is caused by the Eckhaus instability. In a rectangle, some other mechanism is probably responsible. My guess is that a front will form at the leading-edge end wall; if this happens, then it will recede across the cell. Second, are TW states sensitive to sideband modulations at low Rayleigh numbers? In an annulus, the Eckhaus instability would probably cause such a sensitivity. In a rectangle, the Eckhaus instability might be truly absent or just suppressed by the source end wall, and the response of the system would be different. These questions are planned to be addressed in the near future.

Some of the observations presented in this paper can be interpreted in the light of theoretical studies of defect behavior in model systems. Coullet *et al.* [27] studied one-dimensional TW in a two-dimensional system using coupled, cubic, complex Ginzburg-Landau equations (CGLE). Using analytical and numerical techniques, they found solutions in the form of source and sink defects. The wave number downstream was selected by the source, which could move at constant velocity, causing a

Doppler shift. The numerically computed source amplitude profiles were wider than those of the sinks, as in these experiments. van Saarloos and Hohenberg [33] studied a broad class of coherent structures—sources, sinks, pulses, and fronts—in a more general CGLE context. They found that both the cubic and the quintic CGLE generically exhibit a continuous family of sink and front solutions but only a discrete family of sources. In this light, the present experiments would be interpreted by saying that the source defect selects the downstream wave number, and the sink or front that is found on the other side of the cell is simply the member of the continuous family of solutions whose upstream wave number matches that selected by the source. If there is no front or sink solution with the correct upstream wave number, or if the selected wave number lies outside the Eckhaus boundary, then the state cannot be stable. In this interpretation, the Eckhaus instability affects the stability of the TW state outside the defect cores but plays no role in selecting that state. Thus, the Rayleigh number at which the source-sink state decays (Fig. 25) is determined by the stability of the defects and has no connection with the Eckhaus instability, even though the TW far from the defect cores have the wave number and frequency of spatially uniform TW in the middle of the Eckhaus band. Also, the "passivity" of the sink defects in the present experiments corresponds to the existence of a continuum of sink solutions in this context.

Despite the fact that the defects seen in these experiments display some of the properties predicted in work on CGLE models, there is much theoretical work to be done on this subject. First, the theoretical papers cited here make a few comments about the detailed structure near the cores of defects. Second, theorists have hardly begun to consider the role of spatial variations in Rayleigh number that were explored here and especially in I and in Ref. [22]. Finally, it was established in I that the behavior of spatially uniform TW states in this system is not well described by CGLE models. A different theoretical approach will certainly be necessary to explain defect behavior in detail as well.

ACKNOWLEDGMENTS

I would like to thank P. C. Hohenberg, B. I. Shraiman, and H. R. Brand for useful discussions.

[1] M. A. Dominguez-Lerma, D. S. Cannell, and G. Ahlers, Phys. Rev. A **34**, 4956 (1986); G. Ahlers, D. S. Cannell, M. A. Dominguez-Lerma, and R. Heinrichs, Physica D **23**, 202 (1986).

[2] H. Riecke and H. G. Paap, Phys. Rev. A **33**, 547 (1986).

[3] P. Kolodner, preceding paper, Phys. Rev. A **46**, 6431 (1992).

[4] M. S. Heutmaker, P. N. Fraenkel, and J. P. Gollub, Phys. Rev. Lett. **54**, 1369 (1985); G. Ahlers, D. S. Cannell, and V. Steinberg, *ibid.* **54**, 1373 (1985); A. Pocheau, V. Croquette, and P. Le Gal, *ibid.* **55**, 1094 (1985).

[5] S. Kai and K. Hirakawa, Prog. Theor. Phys. Suppl. **64**, 212 (1978); A. Joets and R. Ribotta, J. Phys. (Paris) **47**, 595 (1986).

[6] I. Rehberg, S. Rasenat, and V. Steinberg, Phys. Rev. Lett. **62**, 756 (1989).

[7] E. Bodenschatz, W. Pesch, and L. Kramer, Physica D **32**, 135 (1988); S. Kai and W. Zimmermann, Prog. Theor. Phys. **99**, 458 (1989); J. P. Eckmann and I. Procaccia, Phys. Rev. Lett. **66**, 891 (1991).

[8] G. Goren, I. Procaccia, S. Rasenat, and V. Steinberg, Phys. Rev. Lett. **63**, 1237 (1989).

[9] M. Dubois, R. Da Silva, F. Daviaud, P. Bergé, and A. Petrov, Europhys. Lett. **8**, 135 (1989); J. Hegseth, J. M. Vince, M. Dubois, and P. Bergé, *ibid.* **17**, 413 (1992).

[10] H. R. Brand and R. J. Deissler, Phys. Rev. Lett. **63**, 508 (1989); H. R. Brand and R. J. Deissler, Phys. Rev. A **41**, 5478 (1990).

[11] P. Kolodner, D. Bensimon, and C. M. Surko, Phys. Rev. Lett. **60**, 1723 (1988); D. Bensimon, P. Kolodner, C. M. Surko, H. Williams, and V. Croquette, J. Fluid Mech. **217**, 441 (1990).

[12] A. Joets and R. Ribotta, J. Phys. (Paris) Colloq. **50**, C3-171 (1988); in *Proceedings of the NATO Advanced Research Workshop on New Tends in Nonlinear Dynamics and Pattern Forming Phenomena: The Geometry of Nonequilibrium,* edited by P. Coullet and P. Huerre, NATO Advanced Study Institute Ser. B2, Vol. 237 (Plenum, New York, 1990), p. 125.

[13] Y. Couder, S. Michalland, M. Rabaud, and H. Thomé, in *Proceedings of the NATO Advanced Research Workshop on Nonlinear Evolution of Spatio-Temporal Structures in Dissipative Continuous Systems,* edited by F. H. Busse and L. Kramer, NATO Advanced Study Institute Ser. B2, Vol. 225 (Plenum, New York, 1990), p. 487.

[14] F. H. Busse and J. A. Whitehead, J. Fluid Mech. **66**, 67 (1974).

[15] F. Daviaud, A. Burnol, and O. Ronsin, Europhys. Lett. **16**, 667 (1991); M. Dubois, F. Daviaud, O. Ronsin, and P. Bergé, Physica D (to be published).

[16] A. Pocheau and V. Croquette, J. Phys. (Paris) **45**, 35 (1984).

[17] X. D. Yang, A. Joets, and R. Ribotta, in *Propagation in Systems Far from Equilibrium,* edited by J. E. Wesfreid *et al.* (Springer-Verlag, Berlin, 1988), p. 194.

[18] S. Rasenat, V. Steinberg, and I. Rehberg, Phys. Rev. A **42**, 5998 (1990).

[19] P. Kolodner and H. Williams, in *Proceedings of the NATO Advanced Research Workshop on Nonlinear Evolution of Spatio-Temporal Structures in Dissipative Continuous Systems* (Ref. [13]), p. 73.

[20] S. Rasenat, G. Hartung, B. L. Winkler, and I. Rehberg, Exp. Fluids **7**, 412 (1989).

[21] J. J. Niemela, G. Ahlers, and D. S. Cannell, Phys. Rev. Lett. **64**, 1365 (1990); K. E. Anderson and R. P Behringer, Phys. Lett. A **145**, 323 (1990).

[22] P. Kolodner, Phys. Rev. A **44**, 6448 (1991); **44**, 6466 (1991).

[23] P. Kolodner and J. A. Glazier, Phys. Rev. A **42**, 7504 (1990); J. A. Glazier and P. Kolodner, *ibid.* **43**, 4269

(1991).
[24] P. Kolodner, Phys. Rev. A **42**, 2475 (1990).
[25] C. M Surko and P. Kolodner, Phys. Rev. Lett. **58**, 2055 (1987).
[26] P. Kolodner (unpublished).
[27] P. Coullet, C. Elphick, L. Gil, and J. Lega, Phys. Rev. Lett. **59**, 884 (1987).
[28] The nonconstant velocity of the right-hand front is due to the fact that it is moving through a region of spatially varying Rayleigh number.
[29] K. D. Eaton, D. R. Ohlsen, S. Y. Yamamoto, C. M. Surko, W. Barten, M. Lücke, M. Kamps, and P. Kolodner, Phys. Rev. A **43**, 7105 (1991).
[30] B. L. Winkler and P. Kolodner, J. Fluid Mech. **240**, 31 (1992).
[31] C. M. Surko, D. R. Ohlsen, S. Y. Yamamoto, and P. Kolodner, Phys. Rev. A **43**, 7101 (1991).
[32] W. Barten, M. Lücke, and M. Kamps, Phys. Rev. Lett. **66**, 2621 (1991).
[33] W. van Saarloos and P. C. Hohenberg, Phys. Rev. Lett. **64**, 749 (1990); Physica D **56**, 303 (1992).